

Improved Current Density and Magnetization Reconstruction Through Vector Magnetic Field Measurements

D.A. Broadway^{1,2,3,*}, S.E. Lillie^{1,2}, S.C. Scholten^{1,2}, D. Rohner³, N. Dontschuk¹,
P. Maletinsky³, J.-P. Tetienne^{1,2,†} and L.C.L. Hollenberg^{1,2,‡}

¹*School of Physics, University of Melbourne, Parkville, VIC 3010, Australia*

²*Centre for Quantum Computation and Communication Technology, School of Physics, University of Melbourne, Parkville, VIC 3010, Australia*

³*Department of Physics, University of Basel, Klingelbergstrasse 82, Basel CH-4056, Switzerland*



(Received 15 May 2020; accepted 23 July 2020; published 26 August 2020)

Stray magnetic fields contain significant information about the electronic and magnetic properties of condensed-matter systems. For two-dimensional (2D) systems, stray field measurements can even allow full determination of the source quantity. For instance, a 2D map of the stray magnetic field can be uniquely transformed into the 2D current density that gives rise to the field and, under some conditions, into the equivalent 2D magnetization. However, implementing these transformations typically requires truncation of the initial data and involves singularities that may introduce errors, artefacts, and amplify noise. Here we investigate the possibility of mitigating these issues through vector measurements. For each scenario (current reconstruction and magnetization reconstruction) the different possible reconstruction pathways are analyzed and their performances compared. In particular, we find that the simultaneous measurement of both in-plane components (B_x and B_y) enables near-ideal reconstruction of the current density, without singularity or truncation artefacts, which constitutes a significant improvement over reconstruction based on a single component (e.g., B_z). On the other hand, for magnetization reconstruction, a single measurement of the out-of-plane field (B_z) is generally the best choice, regardless of the magnetization direction. We verify these findings experimentally using nitrogen-vacancy-center magnetometry in the case of a 2D current density and a 2D magnet with perpendicular magnetization.

DOI: [10.1103/PhysRevApplied.14.024076](https://doi.org/10.1103/PhysRevApplied.14.024076)

I. INTRODUCTION

Condensed-matter systems are often accompanied by stray magnetic fields that are the result of uncompensated magnetic moments or the movement of charges in the material. Local magnetic field measurements can therefore be used to investigate the underlying physical phenomena. Stray magnetic fields can be measured using a suitable magnetic probe such as superconducting quantum interference device (SQUID) [1–3], Hall probe [4–6], and nitrogen-vacancy (N-V) centers in diamond [7], arranged either in a dense array or scanning configuration to form a two-dimensional (2D) magnetic field map [8–13]. Using these techniques various physical phenomena have been investigated such as quantum Hall effects [4,14], spin-wave modes [15], magnetism at oxide interfaces [16], 2D magnetic materials [17–22], noncollinear magnetism [23], and domain-wall physics [24,25]. Although less explored,

it is also a promising avenue to study transport phenomena such as viscous electron flow [26], electron guiding and lensing [27,28], spintronics [29], and topological currents [30].

In some cases, it is possible in principle to transform a 2D map of the stray magnetic field into the source quantity [19,20,31–38]. Specifically, a 2D measurement of the stray magnetic field (by convention, in the x - y plane parallel to the sample) can be transformed to obtain a map of 2D current density and, under some conditions, of 2D magnetization. Typically, these 2D measurements are performed such that only a single projection of the stray magnetic field is measured, which is to decrease the total measurement time (N-V [13]) or due to the difficulty in designing a three-axis probe (Hall probe, SQUID [39]). However, the transformation from magnetic field to source quantity contains singularities (undetermined spectral components) that vary depending on the magnetic field direction in question. For example, the transformation from perpendicular magnetic field (B_z) to a 2D out-of-plane magnetization (M_z) contains a single point singularity (the dc Fourier frequency pixel is divided by zero) while the transformation

*davidaaron.broadway@unibas.ch

†jtetienne@unimelb.edu.au

‡lloydch@unimelb.edu.au

from a transverse magnetic field component (B_x or B_y) contains many singularities. Likewise, truncation artefacts arising from the finite lateral size of the measurements (in the x - y plane) are more or less pronounced depending on the measurement direction. Recently, it has been possible to measure the full vector magnetic field directly using ensembles of N-V centers in diamond [11,12,40], which opens opportunities to mitigate these effects in a systematic manner. Here we investigate how this increased information can be used to choose a transformation pathway (e.g., from \mathbf{B} to \mathbf{M}) that minimizes singularity and truncation-induced artefacts.

Several techniques exist to transform the magnetic field into the desired source quantity such as Bayesian inference [34], regularization [32,41], and Fourier-space reconstruction [31,35,36,42]. In this work, we focus on the simplest method of Fourier-space source quantity reconstruction. We compare the use of different magnetic field projections to reconstruct current density, in-plane magnetization, and out-of-plane magnetization. Namely, we analyze the use of Cartesian projections B_x , B_y , B_z , and the projection along an arbitrary direction $B_{\theta,\phi}$, as well as combinations of these magnetic field components. First, in Sec. II, these different magnetic field components are explored for current-density reconstruction for nontrivial current geometries and for regimes where there is a high degree of magnetic field truncation. In Sec. II C, these reconstruction methods are applied to experimental data from a metallic wire fabricated onto an N-V-diamond magnetic imager revealing a clear advantage in using B_x and B_y together. Then in Sec. III, we discuss the transformation from magnetic fields to magnetization and apply these transformations to out-of-plane magnetization in Sec. IV. Here we show that transformations involving transverse magnetic fields have a distinct disadvantage to B_z and in Sec. IV C the results are confirmed by implementing the different reconstruction pathways on experimental data of magnetic flakes of vanadium triiodide (VI_3). Finally, in Sec. V, we investigate in-plane magnetization returning the same conclusion as for out of plane, that B_z is the preferred measurement orientation.

II. RECONSTRUCTION OF CURRENT DENSITY

We first examine the case of current-density reconstruction. Here we show that it is possible to use the in-plane field components together to get a singularity free reconstruction, while using the out-of-plane field leads to a singularity in the transformation. Additionally, we show that there are further artefacts that are introduced due to the longer range of decay of perpendicular magnetic field as compared to the in-plane components for the systems of interest. We demonstrate that these artefacts can change the apparent distribution of the current density in the source material and introduce edge artefacts. Finally,

we demonstrate this variation on experimental data where a clear difference in reconstruction from perpendicular and transverse fields is observed.

A. Theory

The reconstruction of current density from the measured magnetic field can be performed provided the magnetic field is measured in an x - y plane parallel to the confinement plane of the 2D current density (defined as the $z = 0$ plane), with a known height $z' > 0$. Because the current is confined in 2D, the current density has only two vector components, $\mathbf{J} = (J_x, J_y, 0)$. The magnetic field \mathbf{B} is related to \mathbf{J} via the Biot-Savart equation,

$$\mathbf{B}(\mathbf{r}) = \frac{\mu_0}{4\pi} \int d^3\mathbf{r}' \frac{\mathbf{J}(\mathbf{r}') \times (\mathbf{r} - \mathbf{r}')}{|\mathbf{r} - \mathbf{r}'|^3}, \quad (1)$$

where μ_0 is the vacuum permeability and the integration is over all space. This relationship is simplified in Fourier space where the Cartesian components are related by

$$\begin{bmatrix} \mathcal{B}_x \\ \mathcal{B}_y \\ \mathcal{B}_z \end{bmatrix} = \frac{1}{\alpha} \begin{bmatrix} 0 & 1 \\ -1 & 0 \\ ik_y/k & -ik_x/k \end{bmatrix} \begin{bmatrix} \mathcal{J}_x \\ \mathcal{J}_y \end{bmatrix}, \quad (2)$$

where $\mathcal{J}(k_x, k_y)$ is the Fourier-space current density, $\mathcal{B}(k_x, k_y, z')$ is the Fourier-space magnetic field where k_x and k_y are the Fourier-space vector variables with $k = \sqrt{k_x^2 + k_y^2}$. The term $\alpha = 2e^{kz'}/\mu_0$ contains an exponential factor that includes the standoff from the source z' , which acts to reverse propagate the magnetic field to the source plane [35]. When all three field components are known, Eq. (2) is an overconstrained problem, and so there are several ways to deduce \mathcal{J} . An obvious pathway is to use the in-plane field components only (B_x and B_y), which are trivially related to J_x and J_y giving the inverted transformation

$$(B_x, B_y) \rightarrow \begin{cases} \mathcal{J}_x = -\alpha \mathcal{B}_y, \\ \mathcal{J}_y = \alpha \mathcal{B}_x. \end{cases} \quad (3)$$

The inversion expressed by Eq. (3) is complete and contains no singularities, that is, it is defined in the entire k space. An alternative reconstruction pathway is to use B_z only along with the additional condition of $\nabla \cdot \mathbf{J} = 0$ (continuity of current) which gives

$$B_z \rightarrow \begin{cases} \mathcal{J}_x = \frac{\alpha k_y}{ik} \mathcal{B}_z, \\ \mathcal{J}_y = -\frac{\alpha k_x}{ik} \mathcal{B}_z. \end{cases} \quad (4)$$

Although this is the most commonly employed pathway [4,31], one downside is that there exists a singularity at

$k = 0$ where \mathcal{J} is undetermined. In the real space, this corresponds to an unknown overall dc offset of the \mathbf{J} map. For a single field component $B_{\theta,\phi}$ along an arbitrary direction $\mathbf{u} = (u_x, u_y, u_z) = (\sin \theta \cos \phi, \sin \theta \sin \phi, \cos \theta)$, Eq. (4) can be generalized,

$$B_{\theta,\phi} \rightarrow \begin{cases} \mathcal{J}_x = \frac{\alpha k_y}{-u_x k_x - u_y k_y + i u_z k} \mathcal{B}_{\theta,\phi}, \\ \mathcal{J}_y = \frac{\alpha k_x}{u_x k_x + u_y k_y - i u_z k} \mathcal{B}_{\theta,\phi}, \end{cases} \quad (5)$$

where $\mathcal{B}_{\theta,\phi}$ is the Fourier transform of $B_{\theta,\phi}$ and (θ, ϕ) are the spherical angles. Here the transformation in general has the same singularity as the transformation for B_z , that is, \mathcal{J} is undetermined when $k = 0$. In the case of a purely in-plane measurement, e.g., along x , i.e., $\mathbf{u} = (1, 0, 0)$, Eq. (5) becomes $\mathcal{J}_x = -(\alpha k_y / k_x) \mathcal{B}_x$, $\mathcal{J}_y = \alpha \mathcal{B}_x$. The expression for \mathcal{J}_y is the same as in Eq. (3), however \mathcal{J}_x now has many singularities (when $k_x = 0$) stemming from the reduction in available information, seriously compromising the reconstruction. This indicates that, when a single magnetic field projection is measured, it is preferable if this projection has a significant z component to minimize the impact of singularities.

Another aspect to consider is finite-size effects. Indeed, \mathbf{B} is measured over a finite spatial region (in the x - y plane) near the sample, which leads to artefacts in the reconstructed \mathbf{J} when using the above equations. These artefacts are sometimes known as truncation artefacts [42]. To analyze how these vary depending on which \mathbf{B} component is used, we simulate a generic scenario of two current-carrying wires with an angle of $\theta = 10^\circ$ and 60° from the x axis and a standoff of $z' = 50$ nm [Figs. 1(a) and 1(b)]. The simulation has a pixel size of 100 nm where a Gaussian smoothing is applied with a width of 300 nm to mimic the diffraction limit of optical-imaging techniques [13]. While the simulations are performed under these conditions, the results are also valid for scanning systems, which have a higher spatial resolution.

The simulated B_z magnetic field [Fig. 1(c), top panel] is transformed in Fourier space into current density, where initially the $k = 0$ component is set to zero. Then, back in real space, a dc offset is added such that the current density vanishes far from the wires (precisely, we impose that the average current density near the top-left corner be zero). Both the transformation to J_x [Fig. 1(c), bottom-right panel] and J_y [Fig. 1(c), bottom-left panel] have significant edge-related reconstruction errors. The edge artefacts are

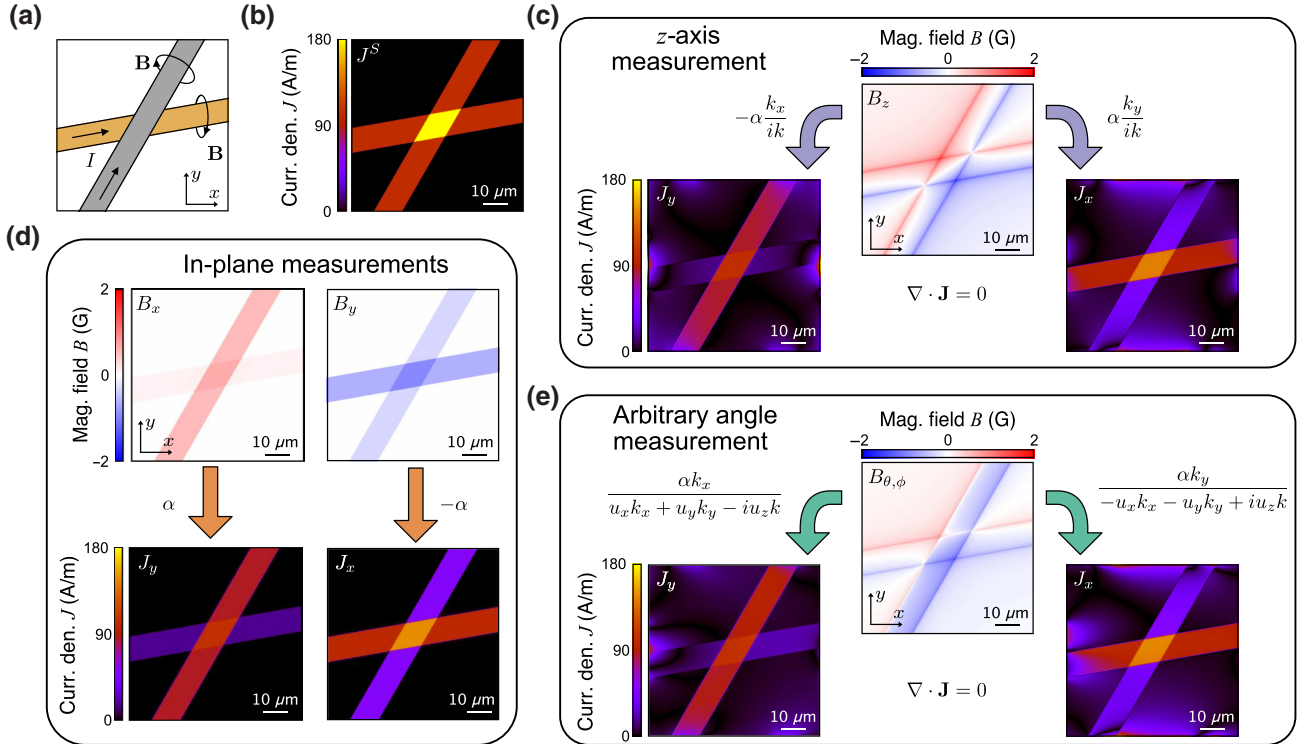


FIG. 1. Reconstruction of current density. (a) Diagram of two independent current-carrying wires (same current I in each) in non-trivial geometry. (b) Simulated current density corresponding to the situation shown in (a) for a current $I = 2$ mA in each wire. (c) Calculated B_z magnetic field (top panel) is then used to reconstruct both J_x and J_y current densities (bottom panels) based on Eq. (4), which assumes that $\nabla \cdot \mathbf{J} = 0$, where the magnitude ($|J_{x,y}|$) is shown for clarity. (d) Calculated B_x and B_y maps (top panels) are used to reconstruct the current density (bottom panels) based on Eq. (3). (e) Calculated $B_{\theta,\phi}$ map (top panel) is used to reconstruct the current density (bottom panels) based on Eq. (5), where $B_{\theta,\phi}$ magnetic field is simulated using $(\theta, \phi) = (54.7^\circ, 45^\circ)$.

related to the way that B_z extends relative to the wire, that is, B_z fields persist significantly beyond the finite window of the measurement. Thus any abrupt end to the magnetic image introduces errors, either along the wire itself, or in the extended field, which introduces magnetic field truncation, which is discussed in the next section. In contrast, the reconstruction from the B_x [Fig. 1(d), left panels] and B_y [Fig. 1(d), right panels] magnetic fields (collectively referred to as B_{xy}) is free of such artefacts. However, in order to perform this reconstruction one either needs to take multiple measurements or use a probe that is sensitive to multiple magnetic field orientation at once, which comes at the cost of signal to noise.

A single measurement with an arbitrary orientation with respect to the sample can also be used to reconstruct the current density. Here we simulate the case of $(\theta, \phi) = (54.7^\circ, 45^\circ)$ which is a common situation in N-V magnetometry using a (100)-oriented diamond [Fig. 1(e)]. However, in this case the measurement suffers from the same truncation errors from the B_z component and the reduced information from the in-plane component. Leading to a very similar current distribution to that of the B_z reconstructed current density.

The truncation affects the low- k components (such that $kz' \ll 1$) which are coarse grained as a result. The transformation for B_z has a $1/k$ factor, which means errors in B_z (low k) are amplified. Meanwhile, the transformation for transverse fields only has the $e^{kz'}$ factor, which is very close to 1 for low k and as such introduces very few truncation artefacts. This is also true in the case of scanning

probes because the size of the image (lowest k) is always much larger than the standoff.

B. Truncation-induced errors

We now analyze these truncation errors in more detail. The truncation of the B_z data depends on the image size in comparison with the size of the wire. This is particularly relevant for scanning sensor systems that typically use small image sizes limited by the long acquisition times involved. While these scanning sensor systems have exceptional resolution for probing small devices [10,43–45], when applied to larger structures the smaller field of view may result in significant truncation. This reduction in field of view for scanning systems is due to a smaller range for the scanning piezos (for low-temperature measurements [19]), the longer measurement time required for a single N-V spins versus ensembles, and the duty cycle of the measurement due to movement time. Due to the slow decay ($1/r$) of the B_z field it is rare to have no truncation and as such in most measurements there is some truncation of the magnetic field [Fig. 2(a)].

The reconstruction of the total current density from the simulated B_z map [Fig. 2(b)] is plagued with edge artefacts due to the truncation of the B_z field. In contrast, the reconstruction from the B_{xy} maps [Fig. 2(c)] has no artefacts and does not require additional processing to improve the reconstruction. The reconstruction from a single arbitrary orientation $(\theta, \phi) = (54.7^\circ, 45^\circ)$ shows a similar error to the case with pure B_z , where they both experience an offset in the wire and outside [Fig. 2(d)]. However, the

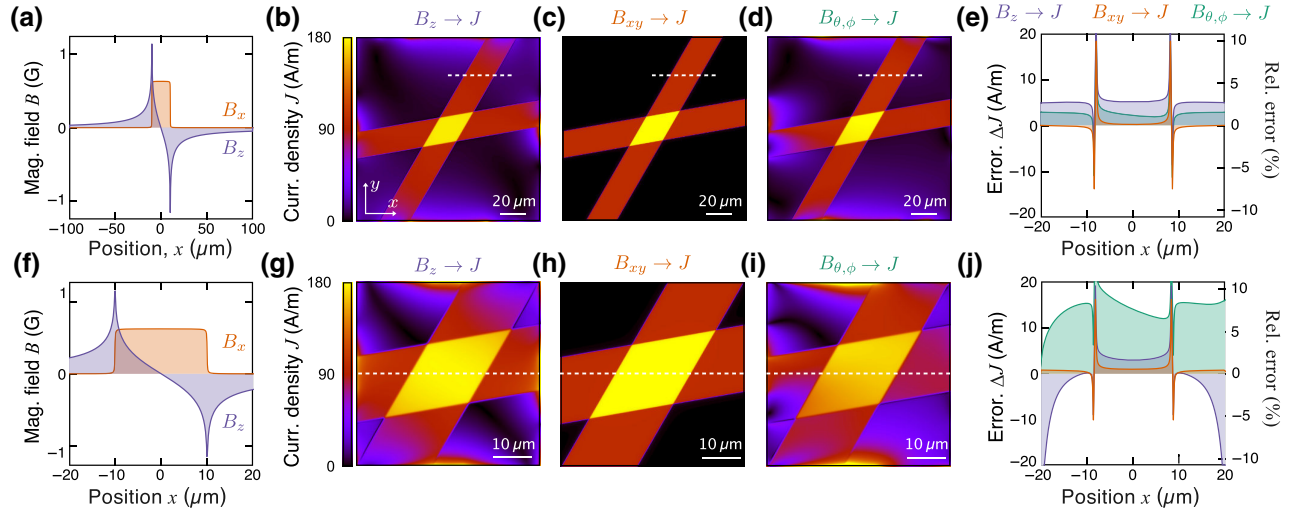


FIG. 2. Truncation errors in current-density reconstruction. (a) Simulated magnetic field from a 20- μm -wide wire with a standoff of 50 nm, orientated along the y direction with a small amount of spatial truncation of B_z . (b)–(d) Current-density norm (J) reconstructed from B_z (b), B_{xy} (c), and $B_{\theta,\phi}$ (d) of the wire geometries in Fig. 1. (e) Line cuts of the difference between the simulated current density and the reconstructed current density for different sources, taken along the dashed line in (b)–(d). The right axis is the relative error normalized to the maximum simulated current density. (f) Magnetic field with a reduced image size. (g)–(i) Reconstructed current density for a measurement confined to the smaller imaging size for B_z (g), B_{xy} (h), and $B_{\theta,\phi}$ (i). (j) Same as (e) but with the reduced image size, taken along the dashed line in (g)–(i). The $B_{\theta,\phi}$ magnetic field is simulated using $(\theta, \phi) = (54.7^\circ, 45^\circ)$.

reconstruction with $B_{\theta,\phi}$ also results in a nonphysical gradient in the wire. Line cuts of the difference between the simulated current (J^S) and the reconstructed current (J^R), $\Delta J = J^S - J^R$, across one of the wires show that even away from the edge effects the reconstruction from B_{xy} more accurately produces the simulated current density than the B_z and $B_{\theta,\phi}$ reconstructions [Fig. 2(e)].

When the image size is reduced further [Fig. 2(f)] the error in reconstruction from B_z increases, particularly near the edges of the image [Fig. 2(g)], while the B_{xy} transformation is unchanged [Fig. 2(h)] and only has issues with edges of the wire due to the finite pixel size in the measurement. The $B_{\theta,\phi}$ reconstruction has an even worse response than the straight B_z reconstruction, due to an asymmetry that is introduced in the reconstructed current density [Fig. 2(i)]. The difference from the simulated current density [Fig. 2(j)] taken along the center of the image shows that reconstruction with B_z can have a deviation of up to 3% in these conditions and $B_{\theta,\phi}$ greater than 10%, relative to the total expected current density (compared to less than 1% in the bulk of the wire for B_{xy}). These deviations are significant and need to be considered when investigating small current effects like edge modes, or spin contributions. Additionally, we perform similar simulations including some noise in the \mathbf{B} data, and find no significant modification of the different reconstruction pathways with the introduction of noise, i.e., the different pathways all returned a similar SNR after reconstruction. We also note that there has been extensive work on how to mitigate the effect of noise in the case of a single-axis measurement [32,34].

In trivial geometries (e.g., single wire in the x direction) the truncation of the magnetic field can be mitigated completely through fitting the magnetic field directly rather than reconstructing the current density [46]. An alternative method involves padding of the real-space image with a linear or exponential decay to extrapolate the data outside the measurement window [42,45]. However, in more complicated geometries this padding is not reliable as the extrapolation introduces additional artefacts. Likewise, simulations of the magnetic tails may involve incorrect assumptions about current distributions and lead to erroneous results. A compromise is to include padding with zeros, which effectively halves the errors due to truncation of the B_z component [42].

A consequence of the truncation artefacts is that they produce a nonuniform background current density where there should be no current at all, which makes it difficult to determine the dc offset in the \mathbf{J} maps, and as a result may bias the estimated current density in the wires themselves. Therefore, it is typically necessary to manually choose a region for zero-point normalization that looks the most artefact free. For instance, in Fig. 2 we choose the top-left corner of the image. Thus, compared with reconstruction from B_{xy} , which requires no normalization

and produces an accurate estimation of the actual current density, reconstruction from B_z and $B_{\theta,\phi}$ is left wanting.

C. Experimental comparison

Experimentally, we validate the simulations using a niobium (Nb) wire fabricated directly on the diamond surface [see photoluminescence image in Fig. 3(a)]. The Nb wire has a thickness of 200 nm and consists of two 200- μm -wide bonding pads that narrow down to a 40- μm -wide channel between them [47]. In order to produce a strong magnetic field, a current of $I = 20$ mA is used. The measurements are taken at room temperature using an ensemble of N- V spins [48] with a depth distribution peaking at 120 nm below the diamond surface [47]. Full details about the diamond sample can be found in Ref. [47]. The Cartesian magnetic field components are obtained by measuring the Zeeman splitting of all four orientations of the N- V spins using optically detected magnetic resonance, where a small bias field of $B = 100$ G is applied to distinctly split all four N- V orientations. In the chosen xyz coordinate system, these four N- V orientations are characterized by spherical angles $\theta = 54.7^\circ$ and $\phi = (\pm 45^\circ, \pm 135^\circ)$, as illustrated in Fig. 3(a). The N- V Hamiltonian can then be used to fit the eight different ODMR frequencies to the three unknown variables B_x, B_y, B_z , as described in detail in previous works [13,49,50]. This provides a reliable way to obtain the vectorial magnetic field components [13,49–51]. The imaging is performed with a custom-built widefield fluorescence microscope [47,52–54]. The vector magnetic field components are shown in Figs. 3(b)–3(d) where a reference measurement is used ($I = 0$) to remove the applied background field. Now we investigate the different current reconstruction pathways with this dataset.

With an image size of $80 \times 80 \mu\text{m}^2$ (only twice the width of the wire) the transverse magnetic fields [Figs. 3(b) and 3(c)] are captured completely while the B_z magnetic field [Fig. 3(d)] is truncated significantly. This is quite explicit in the magnetic field line cuts across [Fig. 3(e)] that show the B_z is still above 25% of the maximum value at the edge of the image. While the current reconstruction from transverse fields [Fig. 3(f)] results in a clear current map with $J = 0$ outside of the wire, the reconstruction from B_z [Fig. 3(g)] has a nonzero background as well as artefacts at the edge of the image. These results are consistent with the simulations in the previous section.

To compare to reconstruction from a single arbitrary direction $B_{\theta,\phi}$ measurement, the same data set is used and the magnetic field map from a single N- V orientation before conversion to B_{xyz} is employed, where the $B_{\theta,\phi}$ map with the least relative noise is chosen (here $(\theta, \phi) \approx (54.7^\circ, 45^\circ)$, although the results are consistent independent of the N- V orientation). The reconstruction from $B_{\theta,\phi}$ produces similar artefacts to the B_z case with additional

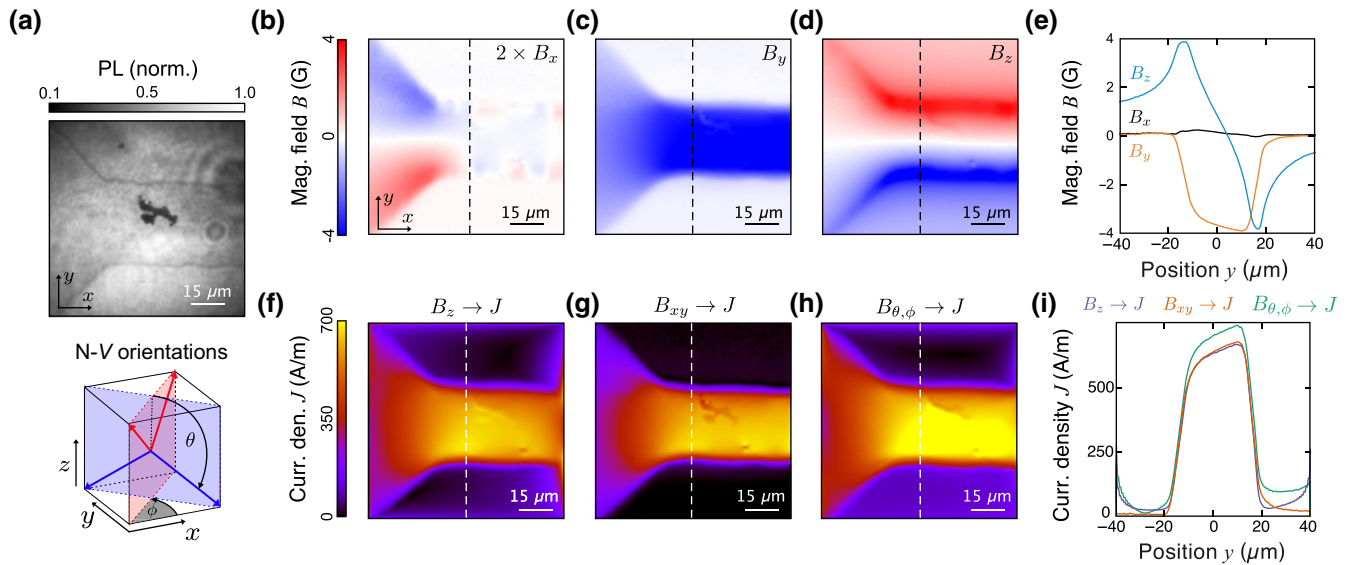


FIG. 3. Experimental example of current reconstruction. (a) N- V photoluminescence image of a Nb wire fabricated directly onto the diamond surface. (b)–(d) Magnetic field images from the Nb wire with a current of $I = 20$ mA deduced from optically detected magnetic resonance (ODMR) spectroscopy. (e) Line cuts of the different magnetic fields, taken along the black dashed line in (b)–(d). (f)–(h) Reconstructed current density norm, J , from B_z (f), B_{xy} (g) and $B_{\theta,\phi}$ (h) magnetic fields. Where the reconstruction with B_{xy} has no padding or additional normalization. Conversely, the reconstruction with B_z and $B_{\theta,\phi}$ is padded with zeros and has a dc offset adjusted in order to cancel J near (but not exactly at) the top edge of the image (see text). (i) Line cuts of the reconstructed current density from different magnetic field sources, taken along the white dashed line in (f)–(h). The $B_{\theta,\phi}$ magnetic field used had an approximate angle of $(\theta, \phi) \approx (54.7^\circ, 45^\circ)$ and the measurements are taken with a background magnetic field of $B = (47.5, 97.4, 19.1)$ G.

gradients caused by the asymmetry in the $B_{\theta,\phi}$ map, leading to a highly nonuniform background [Fig. 3(h)].

To analyze these effects more quantitatively, we look at line cuts taken through the middle of the image [Fig. 3(i)], i.e., away from the edge artefacts. In this regime, the major difference between the different pathways is the amount of current that is attributed to the background, which ultimately changes the integrated current measured depending on the normalization protocol. The total integrated current for the reconstruction from B_{xy} is $I = 20(1)$ mA, which is consistent with the applied $I = 20$ mA. In contrast, the integrated current measured for reconstruction from B_z requires a normalization. To deal with the current outside of the wire one can force $J = 0$ near the edge of the image (zero-point normalization) resulting in a total current density of $I = 21(1)$ mA, which is consistent with the applied value with a slight over estimation due to the edge artefacts. Unlike the reconstruction from B_z , the background from the $B_{\theta,\phi}$ reconstruction is asymmetric about the wire. As a consequence, background normalization becomes even more difficult and even with setting a zero point in the upper background the total integrated current is $I = 24(1)$ mA, which is far from the applied current of $I = 20$ mA. Assumptions about the wire can be used to negate this background in the reconstruction itself, e.g., extrapolation of the magnetic field before transformation, or a background fitting technique can be used to remove

the residual current density after the transformation, but none of these techniques are perfect. Another method is to adjust the offset to match the integrated current (restricting the integral to inside the wire) to the known injected current [46], but this is sensitive to how exactly the edges of the wire are defined and may not be a valid technique for certain current carrying objects.

While current reconstruction from different magnetic field sources results in small differences, these deviations from the actual current density can be crucial for measurements with small SNR or subtle current distribution modifications. To ensure the most reliable result the use of the in-plane magnetic field components is thus preferable. While this is relatively straightforward with widefield imaging [13,52], vector magnetometry with high-resolution scanning N- V systems has not yet been demonstrated. Our results may motivate the development of scanning probes incorporating multiple N- V orientations to enable this.

We note that in the case of N- V spins that are very close to the conductor (< 20 nm), an anomalous reduction in the in-plane field is recently observed, which is currently not understood [42]. As this leads to a clearly erroneous current density, in this case it is preferable to use B_z . We did not observe such an anomaly in the present experiments where the N- V layer had a depth of 120 nm.

It is useful at this stage to discuss the optimal spatial sampling frequency of the magnetic field measurements. Because all reconstruction pathways contain an $\exp(kz')$ term that tends to amplify high-frequency noise, it is best to measure with a spatial frequency that is not more than $1/z'$ (i.e., a step size not less than z'). Sampling at a higher density than this requires the inclusion of filters to remove this noise amplification, which act to effectively reduce the spatial resolution to the standoff distance. Additionally, there is no magnetic field information contained in spatial frequencies above $1/z'$, and as such no information is lost. On the other hand, sampling at a lower density (i.e., with a step size larger than z') results in a loss of information, unless the spatial resolution is not limited by the standoff, which is the case of most widefield measurements. Thus, in order to optimize the spatial resolution of the reconstructed current density, the step size should be taken of the order of the standoff for scanning $N-V$ experiments (typically 50 nm) or of the order of the optical resolution for widefield experiments (e.g., 400 nm in the present experiments). The same rule of thumb applies to magnetization reconstruction, analyzed in the next section.

III. RECONSTRUCTION OF MAGNETIZATION

We now move on to reconstruction of magnetization and examine whether vector measurements may be beneficial. In order to perform the reconstruction we make the assumptions that the magnetization is confined to a 2D plane with a vector $\mathbf{M}(x, y)$ and that the stray field is measured in a parallel plane at a known height z' , $\mathbf{B}(x, y, z')$. The relationship between magnetization and magnetic fields can be greatly simplified in Fourier space [35–38], resulting in

$$\begin{bmatrix} \mathcal{B}_x \\ \mathcal{B}_y \\ \mathcal{B}_z \end{bmatrix} = -\frac{1}{\alpha} \begin{bmatrix} k_x^2/k & k_x k_y/k & i k_x \\ k_x k_y/k & k_y^2/k & i k_y \\ i k_x & i k_y & -k \end{bmatrix} \begin{bmatrix} \mathcal{M}_x \\ \mathcal{M}_y \\ \mathcal{M}_z \end{bmatrix}, \quad (6)$$

where $\mathcal{B}(k_x, k_y, z')$ and $\mathcal{M}(k_x, k_y)$ are the Fourier-space magnetic field and magnetization vectors, respectively, and α is the same as in the current reconstruction, $\alpha = 2e^{kz'}/\mu_0$.

Since the equations for the three different magnetic field components are linearly dependent, there is effectively only one equation that can be used, e.g., $\mathcal{B}_z = f(\mathcal{M}_x, \mathcal{M}_y, \mathcal{M}_z)$, and so there is an infinite number of solutions for \mathcal{M}_x , \mathcal{M}_y , and \mathcal{M}_z . However, in the case where the direction of the \mathbf{M} vector is known and uniform (unit vector \mathbf{u}_M), then we can write $\mathbf{M}(x, y) = \mathbf{u}_M M(x, y)$, where $M(x, y)$ is the scalar amplitude. With only one unknown, it is now possible to use a given component of \mathbf{B} , or a combination of components, to deduce $M(x, y)$.

From Eq. (6), it is clear that there are more singularities than in the current reconstruction case. These singularities can be grouped into three types:

1. $1/k$, single point.
2. $1/k_{x,y}$, singularity line.
3. $1/k_x k_y$, two perpendicular singularity lines.

These singularities in Fourier space correspond to undetermined quantities in real space. For single point singularities ($1/k$), there is an unknown dc offset, which is also present in the current reconstruction except in the B_{xy} pathway. For lines of singularity ($1/k_{x,y}$ or $1/k_x k_y$) there is an unknown offset for every single line of pixels that are parallel to the line of singularity. For example, with a singularity line of $1/k_x$ each line of pixels in the x direction has an unknown and different offset.

In order to form a meaningful real-space image these singularities need to be dealt with such that the gaps of information are closed, i.e., a replacement value for these singularities needs to be picked. For the $1/k$ singularities, just like in the current reconstruction, the condition can be imposed that the real-space magnetization be null away from the magnetic object. For the lines of singularity, this same condition can be imposed however it needs to be determined for each individual line of pixels. Consequently, this normalization procedure adds errors in the presence of noise, measurement errors, and truncation errors. Thus, it is preferable to use the reconstruction pathway that contains as few singularities as possible. This depends on the direction of \mathbf{M} , and so in what follows we examine different situations, starting with the case of pure M_z .

We note that, given the equivalence between current and magnetization, one could also first reconstruct \mathbf{J} by inverting Eq. (2), generalized so as to include an out-of-plane current component J_z , and then deduce \mathbf{M} by inverting $\mathbf{J} = \nabla \times \mathbf{M}$ [36]. However, this two-step method introduces the same singularities as the direct inversion of Eq. (6). Thus, for simplicity we perform the direct inversion.

IV. OUT-OF-PLANE MAGNETIZATION

In the case of magnetic thin films with perpendicular anisotropy, the magnetization can generally be well approximated by a magnetization vector $\mathbf{M}(x, y) = M(x, y)\mathbf{u}_z$, where we ignore the small regions where it may lie in the plane (e.g., in domain walls). In this section, we consider this scenario and analyze the different reconstruction pathways. We then compare these findings with experiments performed on flakes of a van der Waals magnetic material, VI_3 .

A. Theory

The transformation for the different magnetic fields components are given by,

$$\mathcal{M}_z = -\frac{\alpha \mathcal{B}_x}{ik_x}, \quad (7)$$

$$\mathcal{M}_z = -\frac{\alpha \mathcal{B}_y}{ik_y}, \quad (8)$$

$$\mathcal{M}_z = \frac{\alpha \mathcal{B}_z}{k}. \quad (9)$$

From these equations it can be seen that \mathcal{B}_z has a single-point singularity whereas \mathcal{B}_x and \mathcal{B}_y have a line of singularity. However, in the spirit of current reconstruction, it is interesting to examine the possibility of combining B_x and B_y . For instance, we can define a transformation that takes an average of the information afforded by B_x and B_y outside the singularity lines, but use only the singularity-free component otherwise. That is,

$$\mathcal{M}_z = -\alpha \begin{cases} \frac{\mathcal{B}_x}{ik_x} & \text{if } k_y = 0, \\ \frac{\mathcal{B}_y}{ik_y} & \text{if } k_x = 0, \\ \frac{1}{2} \left(\frac{\mathcal{B}_y}{ik_y} + \frac{\mathcal{B}_x}{ik_x} \right) & \text{otherwise.} \end{cases} \quad (10)$$

By combining the two transverse magnetic field components the transformation for B_{xy} now only experiences a single point singularity ($k = 0$) and as such is the technique used going forward along with the B_z pathway. Additionally, for a measurement along a single arbitrary direction (θ, ϕ) , the transformation is

$$\mathcal{M}_z = -\frac{\alpha \mathcal{B}_{\theta,\phi}}{u_x ik_x + u_y ik_y - u_z k}, \quad (11)$$

where $\mathbf{u} = (u_x, u_y, u_z) = (\sin \theta \cos \phi, \sin \theta \sin \phi, \cos \theta)$. In this case, the transformation only has a single point singularity $1/k$, except for the special case where \mathbf{u} coincides with the x or y axis, which we ignore. As all of these pathways ($B_z, B_{xy}, B_{\theta,\phi}$) result in the same style of singularity they are all normalized in the same manner, that is, we impose the condition that the magnetization should be null at the edge of the image (zero-point normalization).

To test the different reconstruction pathways, we simulate the case of two adjacent flakes with uniform magnetization of identical amplitude but opposite signs [Figs. 4(a) and 4(b)]. To simulate conditions that are similar to a wide-field imaging experiment, the simulated \mathbf{B} had a pixel size of 100 nm, which is then convolved with a Gaussian with a width of 300 nm. The magnetic field is calculated with an image size of 30 μm and with a sample to imaging plane standoff of $z' = 50$ nm [Figs. 4(c), 4(e) and 4(g)]. Before applying the inversion, the \mathbf{B} maps are padded with zeros

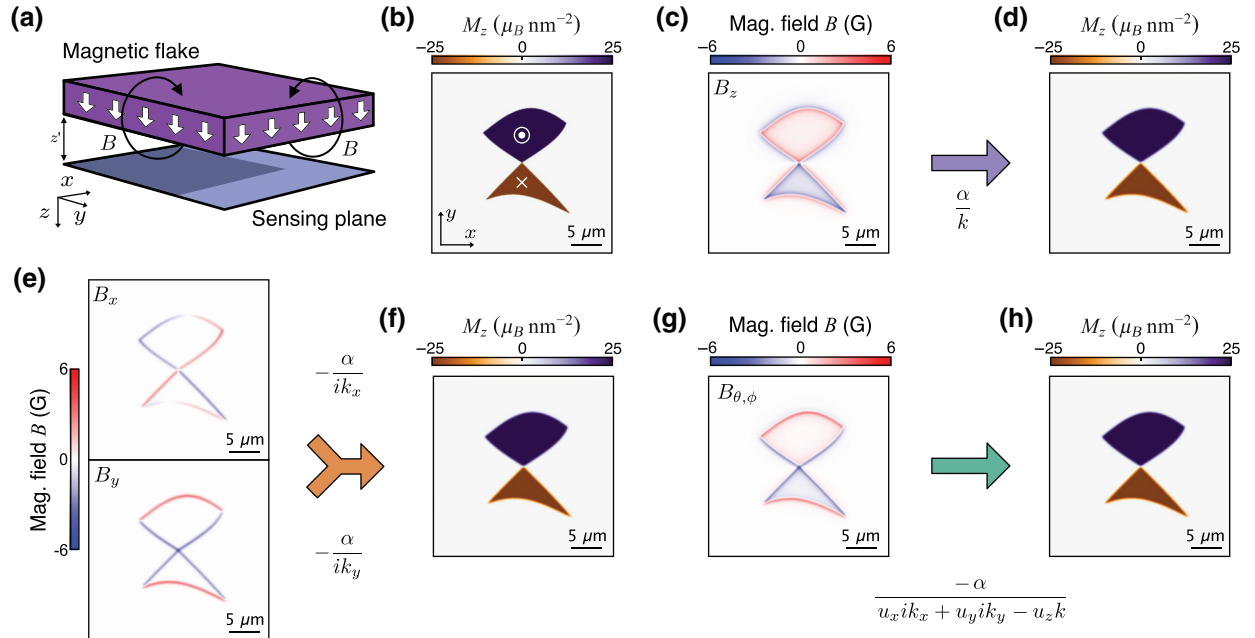


FIG. 4. Reconstruction of out-of-plane magnetization. (a) Diagram of out-of-plane magnetized flake with a sensing plane at a height z' . (b) Assumed magnetization map, where two adjacent flakes have magnetizations of the same amplitude ($M_z = 25 \mu_B \text{nm}^{-2}$) but opposite signs. (c),(d) Calculated B_z map (c) and the reconstruction of M_z (d) using Eq. (9). (e),(f) Calculated B_x and B_y maps (e) and the reconstruction to M_z (f) using the combined magnetic fields [Eq. (10)]. (g),(h) Calculated $B_{\theta,\phi}$ map (g) and the reconstruction to M_z (h) using Eq. (11), with the $B_{\theta,\phi}$ magnetic field simulated using $(\theta, \phi) = (54.7^\circ, 0^\circ)$.

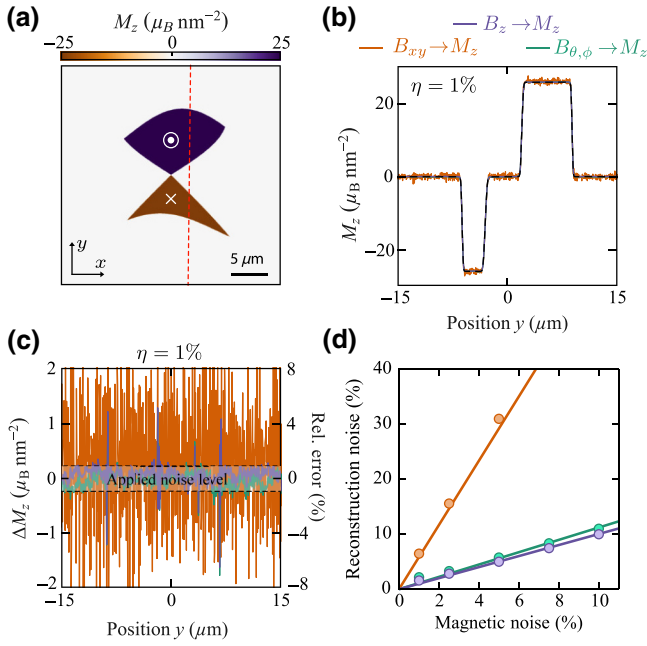


FIG. 5. Effect of noise on reconstruction of out-of-plane magnetization. (a) Simulated magnetization map, identical to Fig. 4(b). (b) Vertical line cut along the red dashed line in (a) for magnetization reconstruction from different magnetic field components (solid lines) and the simulated magnetization (dashed line) with an applied noise of $\eta = 1\%$. The B_z and $B_{\theta,\phi}$ cases are barely visible here but can be better seen in (c). (c) Line cuts of the difference between the simulated and reconstructed magnetization for different magnetic components. The standard deviation of the applied noise is shown as a shaded region between two dashed lines. (d) Simulation of the transformation of the magnetic noise to magnetization noise for different magnetic field components. Linear fits to the data is also shown under the assumption that the two noises converge at zero. The $B_{\theta,\phi}$ magnetic field is simulated using $(\theta, \phi) = (54.7^\circ, 0^\circ)$.

on the outside to decrease edge-related errors. Unlike the magnetic fields from current, the B_z field from a step in M_z does not have a long-range decay and as such truncation is not a significant effect that needs to be considered for widefield experiments. However, in scanning experiments the edge of the image can often cut through a flake and as such has a maximal truncation artefact.

The magnetization reconstruction from the B_z magnetic field [Fig. 4(c)] transforms without any significant artefacts [Fig. 4(d)] as there is no truncation and the zero-point normalization is straightforward. There is a small deviation at the edge of the flake that is due to the Gaussian convolution of the data set. Using Eq. (10), which combines both transverse magnetic field maps [Fig. 4(e)], returns a result that is similar to that of reconstruction from B_z [Fig. 4(f)]. Likewise, reconstruction from $B_{\theta,\phi}$ [Fig. 4(g)] also returns a reliable magnetization [Fig. 4(h)].

B. Noise propagation

Previous work on different reconstruction methods for current density have discussed in detail how noise can affect the reconstruction process [32,34]. To elucidate the differences between the magnetization reconstruction from different magnetic field components, we apply noise to the magnetic field before reconstruction and take vertical line cuts across the flake [Fig. 5(a)] for all the different reconstruction pathways [Fig. 5(b)]. Here we simulate random noise to each pixel in the magnetic field maps, characterized by a standard deviation η defined relative to the maximum field amplitude in the image. Additionally, we remove the Gaussian convolution to compare directly the effect of noise on the transformation without additional treatment. With the introduction of a relatively small error of $\eta = 1\%$ there is a drastic change in the quality of the reconstruction for different magnetic field components [Fig. 5(b)]. When compared to the simulated flake (black dashed line) the reconstructions from B_z and $B_{\theta,\phi}$ perform well, however, reconstruction from B_{xy} has significantly more noise. This noise amplification is quantified by taking the difference between the simulated (M_z^s) and reconstructed (M_z^p) magnetization, $\Delta M_z = M_z^s - M_z^p$ normalized to the assumed magnetization amplitude [Fig. 5(c)]. The error in the reconstructed magnetization shows that reconstruction from B_{xy} is the least robust to noise, taking the initial noise of 1% and returning noise $> 4\%$. In contrast, the other reconstruction pathways have a significantly better response and maintain a similar noise level. In principle, techniques can be used to minimize the error on the reconstruction from B_{xy} , as is used for in-plane magnetization, but they come at the cost of spatial resolution.

The transformation of the magnetic field noise to magnetization noise has a linear response [Fig. 5(d)], where reconstruction from both B_z and $B_{\theta,\phi}$ fields closely mirrors the applied noise, while B_{xy} drastically amplifies it. The linear amplification of the noise is expected due to the linear nature of the operations realized in all the reconstruction pathways. The difference in the reconstruction is partially due to the transverse magnetic field maps being more sparsely filled than B_z which results in a difference in the effective SNR after transformation. It is important to note that in an experiment with (100)-orientated diamond, B_z is obtained through full vector ODMR spectroscopy, which has a worse SNR than a single N-V measurement, and as such may in practice perform worse. Lastly, in the case of truncated fields, the symmetry of the B_z magnetic field map translates to a symmetric erroneous background magnetization, whereas due to the orientation of $B_{\theta,\phi}$ the background magnetic field is asymmetric. Both forms of background magnetizations can be removed through an appropriate background subtraction, but different approaches may be required as is the case in current reconstruction.

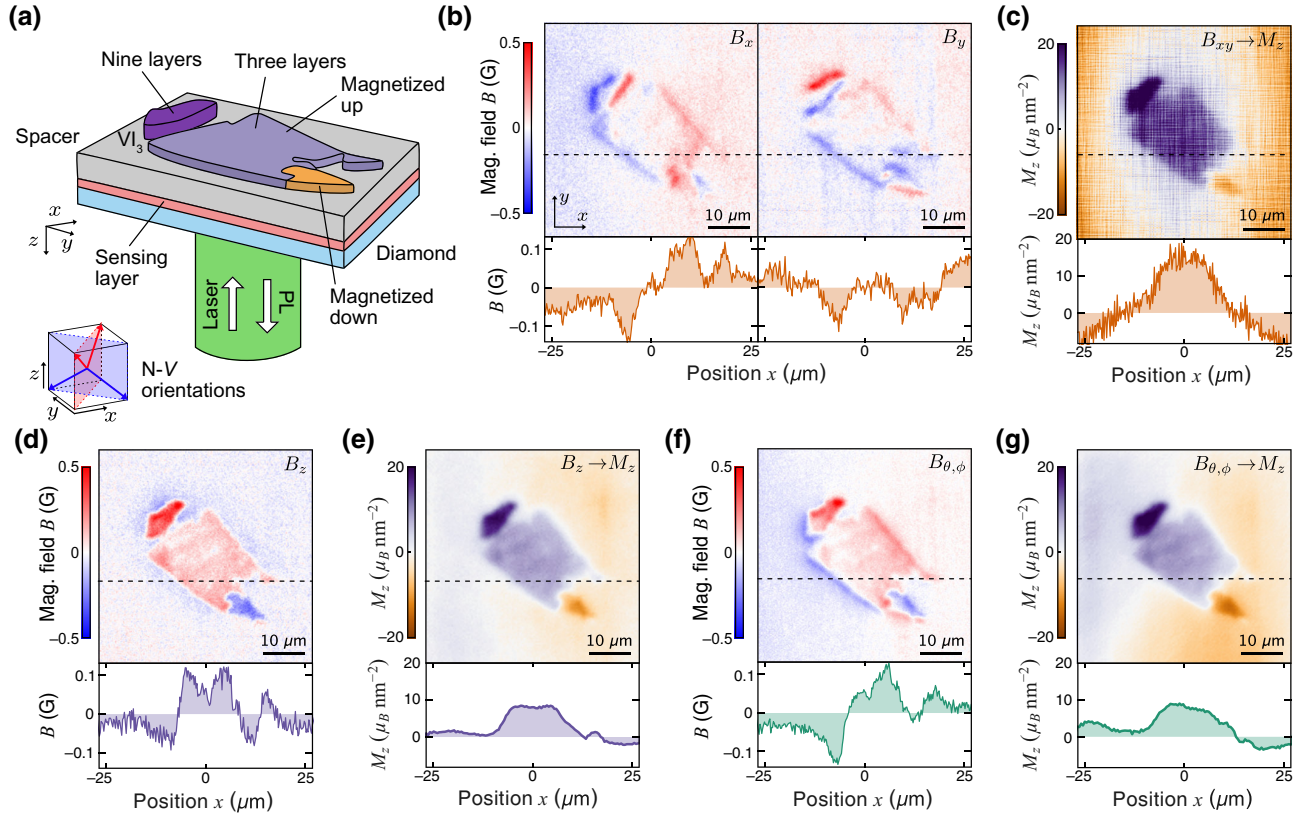


FIG. 6. Experimental example of reconstruction of out-of-plane magnetization. (a) Schematic of experimental setup where magnetic VI_3 flakes are placed onto the diamond surface. The optical excitation and photoluminescence readout is performed through the diamond substrate. (b) Transverse magnetic field components, B_x and B_y , obtained from full vector ODMR spectroscopy. (c) Reconstruction of out-of-plane magnetization from the transverse magnetic fields. (d) B_z magnetic field obtained from the same full vector ODMR measurement as in (b). (e) Reconstruction of out-of-plane magnetization from the B_z magnetic field. (f) $B_{\theta,\phi}$ from a single N-V axis with a direction of $(\theta,\phi) = (54.7^\circ, 45^\circ)$. (g) Reconstruction of out-of-plane magnetization from the $B_{\theta,\phi}$ magnetic field. In (b)–(g), below each map is a line cut taken along the dashed line shown on the map. The measurements are taken with a background magnetic field of $B = (21, 44, 41.5)$ G.

For both ensemble N-V imaging [13] and scanning N-V microscopy [10] reconstruction from B_z offers the best transformation potential. As a consequence, (111)-orientated diamond imaging platforms offer both the best transformation and the best signal to noise ratio by not requiring full vector magnetometry. Bulk diamond slabs with (111) orientation are commercially available and recently (111)-diamond atomic force microscope (AFM) scanning tips have been fabricated [55]. However, $B_{\theta,\phi}$ does perform very similarly in (100)-orientated diamond and is appropriate for most sensing scenarios.

C. Experimental comparison

Experimentally, we validate the simulations using a flake of VI_3 [56–58] placed onto the diamond [Fig. 6(a)], where the description of the fabrication process can be found in Ref. [20]. The measurements are taken using an N-V layer similar to that used for current reconstruction in Sec. II C. The measurements are performed at a

temperature of $T = 5$ K under a bias field of $B = 120$ G to distinctly split all four N-V orientations and are taken using a custom-built closed-cycle cryostat widefield fluorescence microscope [47]. The magnetic field components are obtained in the same fashion as in the measurements of the Nb wire (Sec. II C).

The magnetic field maps are shown in Figs. 6(b), 6(d), and 6(f), where the bias field is removed by subtracting the mean value of each map. The corresponding reconstructed magnetization M_z maps are shown in Figs. 6(c), 6(e), and 6(g). Due to the transformation for the transverse magnetic fields amplifying the noise, the reconstruction from this pathway is littered with additional artefacts [Fig. 6(c)]. In contrast, the reconstruction from the B_z magnetic field produces a relatively uniform near-zero background and a clear domain structure in the flake [Fig. 6(e)]. This is also in contrast to the reconstruction from the $B_{\theta,\phi}$ magnetic field [Fig. 6(g)] taken with an N-V with an orientation of $(\theta,\phi) = (54.7^\circ, 45^\circ)$. The $B_{\theta,\phi}$ magnetic field has a gradient in the measurement (presumably an artefact arising from

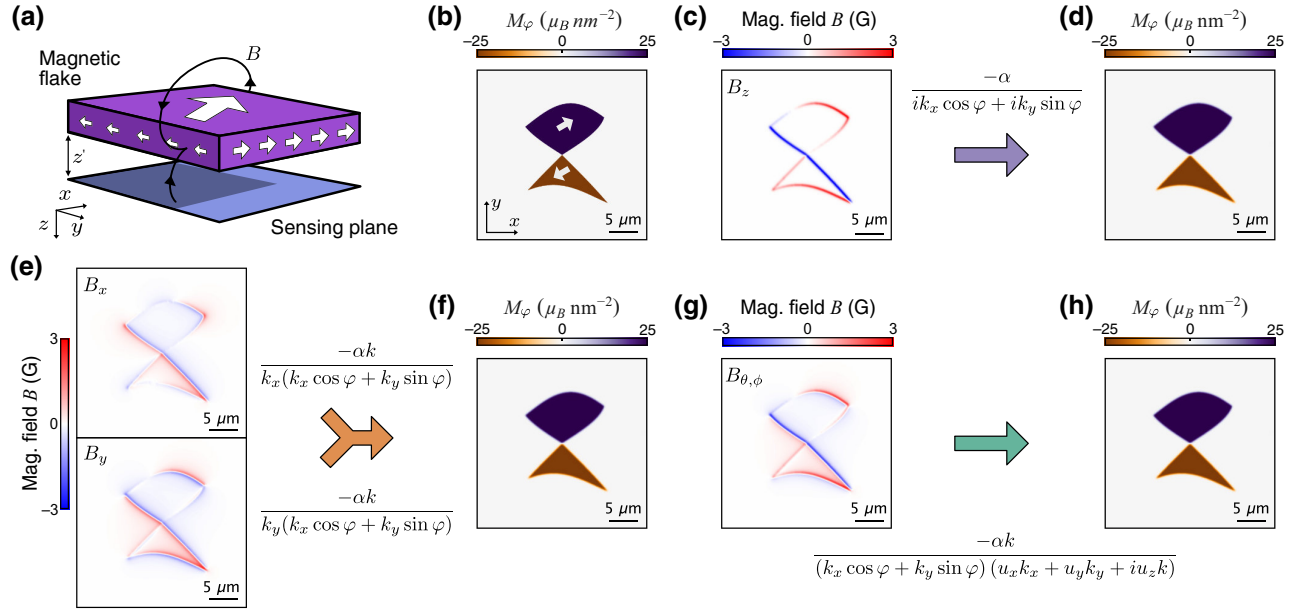


FIG. 7. Reconstruction of in-plane magnetization. (a) Diagram of magnetic flake with in-plane magnetization at $\varphi = 30^\circ$ with a sensing plane. (b) Assumed magnetization map, corresponding to two adjacent flakes with opposite magnetization as denoted by the arrows. (c),(d) Calculated B_z map (c) and the reconstruction of M_φ (d) using Eq. (14). (e),(f) Calculated B_x and B_y maps (e) and the reconstruction to M_φ (f) using the combined magnetic fields [Eq. (15)]. (g),(h) Calculated $B_{\theta,\phi}$ map (g) and the reconstruction to M_φ (h) using Eq. (16), with $(\theta, \phi) = (54.7^\circ, 45^\circ)$.

the ODMR fitting) that when reconstructing to magnetization generates a (nonphysical) background magnetization that hinders quantitative analysis of the magnetization inside the flake. Although there are strategies to remove this background, B_z seems to offer a more reliable reconstruction, particularly in cases where there are additional nearby flakes, whose interfering magnetic field may inhibit such techniques.

Here we find that without additional processing, only reconstruction of out-of-plane magnetization using the B_z magnetic field is able to reconstruct the magnetization of the flake such that there are clearly distinguishable magnetic domains with relatively uniform magnetization in each. Our results thus confirm that B_z is the best choice for reconstructing out-of-plane magnetization if available or reconstruction from $B_{\theta,\phi}$ if additional stray background magnetic fields are minimized.

V. IN-PLANE MAGNETIZATION

We now move to the case of an in-plane magnetization. Here the magnetization can be reconstructed from the stray magnetic field only for a system with in-plane uniaxial anisotropy so that the magnetization vector has a fixed and known direction throughout the sample. We analyze the different pathways to perform this reconstruction and discuss the singularities involved and how they are affected by noise.

The in-plane magnetization has a more complex transformation from magnetic field as can be seen from the total transformation given in Eq. (6). The magnetization vector can be expressed as $\mathbf{M} = M_\varphi [\cos(\varphi), \sin(\varphi), 0]$ where M_φ is the amplitude and φ is the angle of \mathbf{M} with respect to the x axis. The transformations take the form of

$$\mathcal{M}_\varphi^x = -\frac{\alpha k \mathcal{B}_x}{k_x(k_x \cos \varphi + k_y \sin \varphi)}, \quad (12)$$

$$\mathcal{M}_\varphi^y = -\frac{\alpha k \mathcal{B}_y}{k_y(k_x \cos \varphi + k_y \sin \varphi)}, \quad (13)$$

$$\mathcal{M}_\varphi^z = -\frac{\alpha \mathcal{B}_z}{ik_x \cos \varphi + ik_y \sin \varphi}. \quad (14)$$

These transformations all exhibit a singularity line that is related to the angle of magnetization, i.e., when $k_x = -k_y \tan \varphi$. The transverse magnetic field transformations also have an additional singularity line when $k_x = 0$ for B_x and when $k_y = 0$ for B_y . This additional singularity is circumvented in the same way as in the out-of-plane magnetization by combining the two cases,

$$\mathcal{M}_\varphi^{x,y} = \begin{cases} \mathcal{M}_\varphi^x & \text{if } k_y = 0, \\ \mathcal{M}_\varphi^y & \text{if } k_x = 0, \\ \frac{1}{2} (\mathcal{M}_\varphi^x + \mathcal{M}_\varphi^y) & \text{otherwise,} \end{cases} \quad (15)$$

returning the transformation to the same singularities as B_z . To bypass the singularities we set each point along this singularity line by imposing that each corresponding oblique linecut in the real-space M_φ map have a vanishing baseline, based on the fact that there should be no magnetization outside the flake. Therefore, the presence of noise and errors in the B maps (e.g., background gradients) translates into an error in each of these offsets, unlike M_z where only the global offset is uncertain. Reconstruction from $B_{\theta,\phi}$ can also be used and takes the more complex form,

$$\mathcal{M}_\varphi^{\theta,\phi} = \frac{-\alpha k \mathcal{B}_{\theta,\phi}}{(k_x \cos \varphi + k_y \sin \varphi) (u_x k_x + u_y k_y + i u_z k)}, \quad (16)$$

which has the same singularities ($k_x = -k_y \tan \varphi$) as the other transformations.

The reconstruction methods are tested by simulating considering two oppositely magnetized flakes in close proximity with an angle of $\varphi = 30^\circ$ from the x axis [Figs. 7(a) and 7(b)], where it is assumed that we know the angle of the magnetization for the reconstruction. In principle, for a single domain it is possible to determine the angle through reconstruction from different angles and excluding nonphysical results. The different reconstruction pathways in the absence of noise all perform similarly, where reconstruction from B_z [Figs. 7(c) and 7(d)], B_{xy} [Figs. 7(e) and 7(f)], and $B_{\theta,\phi}$ [Figs. 7(g) and 7(h)] all perform well with a blurring of the flake edge due to the imposed diffraction limit of 300 nm.

To illustrate the effect of noise we take vertical line cuts across the flakes [Fig. 8(a)]. The inclusion of a small random noise $\eta = 1\%$ in the magnetic field images results in a similar response across all pathways [Fig. 8(b)]. However, unlike in the case of out-of-plane magnetization here the noise in the magnetization is amplified compared to the magnetic field noise, by a factor 2–3 [Fig. 8(c)]. The linear scaling of the noise from the different reconstructions indicates that the B_z transformation is the most robust, although it still amplifies the noise by more than a factor of 2 [Fig. 8(d)]. We note that the noise amplification greatly depends on the type of filter one applies to the transformation. In this case we apply an Hanning filter with a low-pass filter to remove oscillations that are faster than $1/z'$. However, one could apply stricter filters at the loss of spatial resolution to reduce the noise further. These results suggest that reconstruction from the B_z magnetic field component has an advantage to other components due to it being slightly more robust to noise. This is particularly relevant for scenarios with a low signal to noise or subtle edge effects.

Note that the reconstruction methods presented above can in principle be extended to an arbitrary magnetization direction that is neither in plane nor out of plane. As both of these special cases show that B_z returns the most

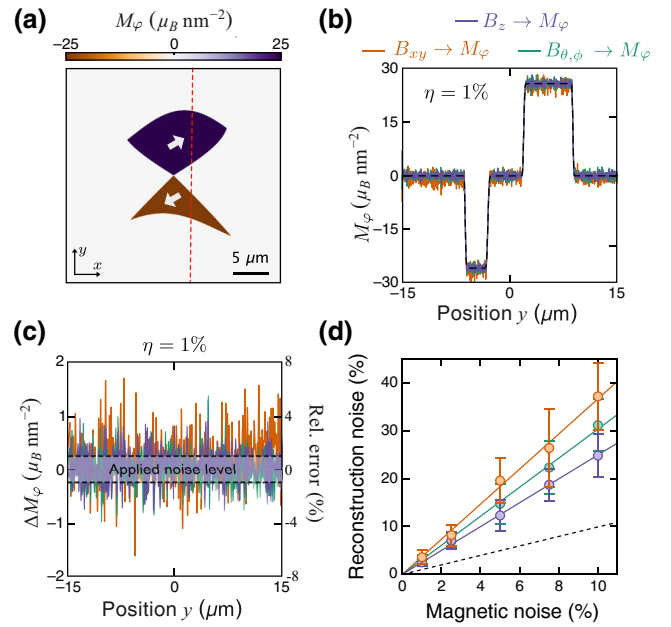


FIG. 8. Effect of noise on reconstruction of in-plane magnetization. (a) Simulated magnetization map, identical to Fig. 7(b) with an angle of $\varphi = 30^\circ$. (b) Vertical line cut along the red dashed line in (a) for magnetization reconstruction from different magnetic field components with a relative noise $\eta = 1\%$ (solid lines) and the simulated magnetization (dashed line). The B_z and $B_{\theta,\phi}$ cases are barely visible here but can be better seen in (c). (c) Line cuts of the difference between the simulated and reconstructed magnetization for different magnetic components. The standard deviation of the applied field noise is shown as a shaded region between two dashed lines. (d) Simulation of the transformation of the magnetic field noise to magnetization noise for different magnetic field components, where the error bars represent the standard deviation in the reconstructed noise over multiple different simulations. The magnetic field noise level is shown as a black dashed line and linear fits to the data is also shown under the assumption that the two noises converge at zero. The $B_{\theta,\phi}$ magnetic field is simulated using $(\theta,\phi) = (54.7^\circ, 0^\circ)$.

error tolerant result, B_z is also the best choice for any other orientation.

VI. CONCLUSION

In this work we investigate how 2D maps of stray magnetic fields can be used to reconstruct the source quantity, focusing on the comparison between the different pathways afforded by vector information. Additionally, we investigate the same reconstructions with an arbitrary projection of the magnetic field ($B_{\theta,\phi}$). In the case of reconstruction of current density, we find that the combination of B_x and B_y magnetic field maps provides a near-ideal transformation, while B_z and $B_{\theta,\phi}$ measurements lead to edge artefacts due to truncation of the long-range B_z magnetic field, which is particularly prone to error for small image sizes, which are commonly used in scanning experiments. These results

are confirmed experimentally by performing the reconstruction from different magnetic field components from a current-carrying wire with a widefield N- V microscope. These findings motivate the development of N- V scanning probes with vector capability, which enables high spatial resolution, high-accuracy imaging of transport processes.

In the case of magnetization reconstruction, we find that using the combination of B_x and B_y leads to a significant amplification of noise. As a consequence this reconstruction pathway is undesirable when compared with B_z and $B_{\theta,\phi}$, which both produce a relatively similar quality for reconstruction of magnetization. Independent of the magnetization direction, we find that reconstruction from the B_z magnetic field component is the most robust to noise and thus the preferred reconstruction pathway. We confirm these results through performing magnetization reconstruction on perpendicularly magnetized flakes using a widefield N- V microscope. These findings motivate the use of (111)-oriented diamond with out-of-plane orientated N- V s for magnetization mapping [55].

ACKNOWLEDGMENTS

The authors thank B.C. Johnson for assistance with the preparation of diamond samples, C. Tan, G. Zheng, L. Wang, S. Tian, C. Li, and H. Lei for providing the VI_3 samples (described in Ref. [20]) and L. Thiel for useful discussions. We acknowledge support from the Australian Research Council (ARC) through Grants No. FL130100119, No. DE170100129, No. CE170100012, No. LE180100037, and No. DP190101506. D.A.B. and S.E.L. are supported by an Australian Government Research Training Program Scholarship.

-
- [1] Yanmeng Shi, Joshua Kahn, Ben Niu, Zaiyao Fei, Bosong Sun, Xinghan Cai, Brian A. Francisco, Di Wu, Zhi-Xun Shen, Xiaodong Xu, David H. Cobden, and Yong-Tao Cui, Imaging quantum spin Hall edges in monolayer WTe₂, *Sci. Adv.* **5**, eaat8799 (2019).
- [2] Denis Vasyukov, Yonathan Anahory, Lior Embon, Dorri Halbertal, Jo Cuppens, Lior Neeman, Amit Finkler, Yehonathan Segev, Yuri Myasoedov, Michael L. Rappaport, Martin E. Huber, and Eli Zeldov, A scanning superconducting quantum interference device with single electron spin sensitivity, *Nat. Nanotechnol.* **8**, 639 (2013).
- [3] Beena Kalisky, Eric M. Spanton, Hilary Noad, John R. Kirtley, Katja C. Nowack, Christopher Bell, Hiroki K. Sato, Masayuki Hosoda, Yanwu Xie, Yasuyuki Hikita, Carsten Woltmann, Georg Pfanzelt, Rainer Jany, Christoph Richter, Harold Y. Hwang, Jochen Mannhart, and Kathryn A. Moler, Locally enhanced conductivity due to the tetragonal domain structure in LaAlO₃/SrTiO₃ heterointerfaces, *Nat. Mater.* **12**, 1091 (2013).
- [4] Katja C. Nowack, Eric M. Spanton, Matthias Baenninger, Markus König, John R. Kirtley, Beena Kalisky, C. Ames, Philipp Leubner, Christoph Brüne, Hartmut Buhmann, Laurens W. Molenkamp, David Goldhaber-Gordon, and Kathryn A. Moler, Imaging currents in HgTe quantum wells in the quantum spin Hall regime, *Nat. Mater.* **12**, 787 (2013).
- [5] Rafael B. Dinner, Kathryn A. Moler, D. Matthew Feldmann, and M. R. Beasley, Imaging ac losses in superconducting films via scanning Hall probe microscopy, *Phys. Rev. B* **75**, 144503 (2007).
- [6] Rafael B. Dinner, Kathryn A. Moler, M. R. Beasley, and D. Matthew Feldmann, Enhanced current flow through meandering grain boundaries in YBa₂Cu₃O_{7- δ} films, *Appl. Phys. Lett.* **90**, 212501 (2007).
- [7] Marcus W. Doherty, Neil B. Manson, Paul Delaney, Fedor Jelezko, Jörg Wrachtrup, and Lloyd C. L. Hollenberg, The nitrogen-vacancy colour centre in diamond, *Phys. Rep.* **528**, 1 (2013).
- [8] L. Rondin, J.-P. Tetienne, T. Hingant, J.-F. Roch, P. Maletinsky, and V. Jacques, Magnetometry with nitrogen-vacancy defects in diamond, *Reports Prog. Phys.* **77**, 056503 (2014).
- [9] L. Rondin, J.-P. Tetienne, P. Spinicelli, C. Dal Savio, K. Karrai, G. Dantelle, A. Thiaville, S. Rohart, J.-F. Roch, and V. Jacques, Nanoscale magnetic field mapping with a single spin scanning probe magnetometer, *Appl. Phys. Lett.* **100**, 153118 (2012).
- [10] P. Maletinsky, S. Hong, M. S. Grinolds, B. Hausmann, M. D. Lukin, R. L. Walsworth, M. Loncar, and A. Yacoby, A robust scanning diamond sensor for nanoscale imaging with single nitrogen-vacancy centres, *Nat. Nanotechnol.* **7**, 320 (2012).
- [11] S. Steiner, F. Dolde, P. Neumann, A. Aird, B. Naydenov, G. Balasubramanian, F. Jelezko, and J. Wrachtrup, High sensitivity magnetic imaging using an array of spins in diamond, *Rev. Sci. Instrum.* **81**, 43705 (2010).
- [12] L. M. Pham, D. Le Sage, P. L. Stanwix, T. K. Yeung, D. Glenn, A. Trifonov, P. Cappellaro, P. R. Hemmer, Mikhail D. Lukin, H. Park, A. Yacoby, and Ronald L. Walsworth, Magnetic field imaging with nitrogen-vacancy ensembles, *New J. Phys.* **13**, 045021 (2011).
- [13] Jean-Philippe Tetienne, Nikolai Dotschuk, and David A. Broadway, Alastair Stacey, David A. Simpson, and Lloyd C. L. Hollenberg: Quantum imaging of current flow in graphene, *Sci. Adv.* **3**, e1602429 (2017).
- [14] Aviram Uri, Youngwook Kim, Kousik Bagani, Cyprian K. Lewandowski, Sameer Grover, Nadav Auerbach, Ella O. Lachman, Yuri Myasoedov, Takashi Taniguchi, Kenji Watanabe, Jurgen Smet, and Eli Zeldov, Nanoscale imaging of equilibrium quantum Hall edge currents and of the magnetic monopole response in graphene, *Nat. Phys.* **16**, 164 (2020).
- [15] Chunhui Du, Toeno van der Sar, Tony X. Zhou, Pramey Upadhyaya, Francesco Casola, Huiliang Zhang, Mehmet C. Onbasli, Caroline A. Ross, Ronald L. Walsworth, Yaroslav Tserkovnyak, and Amir Yacoby, Control and local measurement of the spin chemical potential in a magnetic insulator, *Science* **357**, 195 (2017).
- [16] Y. Anahory, L. Embon, C. J. Li, S. Banerjee, A. Meltzer, H. R. Naren, A. Yakovenko, J. Cuppens, Y. Myasoedov, M.

- L. Rappaport, M. E. Huber, K. Michaeli, T. Venkatesan, Ariando, and E. Zeldov, Emergent nanoscale superparamagnetism at oxide interfaces, *Nat. Commun.* **7**, 12566 (2016).
- [17] M. Gibertini, M. Koperski, A. F. Morpurgo, and K. S. Novoselov, Magnetic 2D materials and heterostructures, *Nat. Nanotechnol.* **14**, 408 (2019).
- [18] Cheng Gong and Xiang Zhang, Two-dimensional magnetic crystals and emergent heterostructure devices, *Science* **363**, 706 (2019).
- [19] L. Thiel, Z. Wang, M. A. Tschudin, D. Rohner, I. Gutiérrez-Lezama, N. Ubrig, M. Gibertini, E. Giannini, A. F. Morpurgo, and P. Maletinsky, Probing magnetism in 2D materials at the nanoscale with single-spin microscopy, *Science* **364**, 973 (2019).
- [20] David A. Broadway, Sam C. Scholten, Cheng Tan, Nikolai Donschuk, Scott E. Lillie, Brett C. Johnson, Guolin Zheng, Zhenhai Wang, Artem R. Oganov, Shangjie Tian, Chenghe Li, Hechang Lei, Lan Wang, Lloyd C. L. Hollenberg, and Jean-Philippe Tetienne, Imaging domain reversal in an ultrathin van der Waals ferromagnet, preprint: arXiv:2003.08470 (in press).
- [21] M. S. Wörmle, P. Welter, Z. Kašpar, K. Olejník, V. Novák, R. P. Campion, P. Wadley, T. Jungwirth, C. L. Degen, and P. Gambardella, Current-induced fragmentation of antiferromagnetic domains, preprint arXiv:1912.05287.
- [22] M. Kim, P. Kumaravadeivel, J. Birkbeck, W. Kuang, S. G. Xu, D. G. Hopkinson, J. Knolle, P. A. McClarty, A. I. Berdyugin, M. Ben Shalom, R. V. Gorbachev, S. J. Haigh, S. Liu, J. H. Edgar, K. S. Novoselov, I. V. Grigorieva, and A. K. Geim, Micromagnetometry of two-dimensional ferromagnets, *Nat. Electron.* **2**, 457 (2019).
- [23] I. Gross, W. Akhtar, V. Garcia, L. J. Martínez, S. Chouaieb, K. Garcia, C. Carrétéro, A. Barthélémy, P. Appel, P. Maletinsky, J.-V. Kim, J. Y. Chauleau, N. Jaouen, M. Viret, M. Bibes, S. Fusil, and V. Jacques, Real-space imaging of non-collinear antiferromagnetic order with a single-spin magnetometer, *Nature* **549**, 252 (2017).
- [24] J.-P. Tetienne, T. Hingant, J. V. Kim, L. H. Diez, J. P. Adam, K. Garcia, J. F. Roch, S. Rohart, A. Thiaville, D. Ravelosona, and V. Jacques, Nanoscale imaging and control of domain-wall hopping with a nitrogen-vacancy center microscope, *Science* **344**, 1366 (2014).
- [25] J.-P. Tetienne, T. Hingant, L. J. Martínez, S. Rohart, A. Thiaville, L. Herrera Diez, K. Garcia, J.-P. Adam, J.-V. Kim, J.-F. Roch, I. M. Miron, G. Gaudin, L. Vila, B. Ocker, D. Ravelosona, and V. Jacques, The nature of domain walls in ultrathin ferromagnets revealed by scanning nanomagnetometry, *Nat. Commun.* **6**, 6733 (2015).
- [26] D. A. Bandurin, I. Torre, R. K. Kumar, M. Ben Shalom, A. Tomadin, A. Principi, G. H. Auton, E. Khestanova, K. S. Novoselov, I. V. Grigorieva, L. A. Ponomarenko, A. K. Geim, and M. Polini, Negative local resistance caused by viscous electron backflow in graphene, *Science* **351**, 1055 (2016).
- [27] Vadim V. Cheianov, Vladimir Fal'ko, and B. L. Altshuler, The focusing of electron flow and a veselago lens in graphene p-n junctions, *Science* **315**, 1252 (2007).
- [28] Shaowen Chen, Zheng Han, Mirza M. Elahi, K. M. Masum Habib, Lei Wang, Bo Wen, Yuanda Gao, Takashi Taniguchi, Kenji Watanabe, James Hone, Avik W. Ghosh, and Cory R. Dean, Electron optics with p-n junctions in ballistic graphene, *Science* **353**, 1522 (2016).
- [29] T. Jungwirth, X. Marti, P. Wadley, and J. Wunderlich, Antiferromagnetic spintronics, *Nat. Nanotechnol.* **11**, 231 (2016).
- [30] R. V. Gorbachev, J. C. W. Song, G. L. Yu, A. V. Kretinin, F. Withers, Y. Cao, A. Mishchenko, I. V. Grigorieva, K. S. Novoselov, L. S. Levitov, and A. K. Geim, Detecting topological currents in graphene superlattices, *Science* **346**, 448 (2014).
- [31] Bradley J. Roth, Nestor G. Sepulveda, and John P. Wikswo, Using a magnetometer to image a two-dimensional current distribution, *J. Appl. Phys.* **65**, 361 (1989).
- [32] Alexander Y. Meltzer, Eitan Levin, and Eli Zeldov, Direct Reconstruction of Two-Dimensional Currents in Thin Films from Magnetic-Field Measurements, *Phys. Rev. Appl.* **8**, 064030 (2017).
- [33] L. A. Knauss, A. B. Cawthorne, N. Lettsome, S. Kelly, S. Chatrathorn, E. F. Fleet, F. C. Wellstood, and W. E. Vandervlinde, Scanning SQUID microscopy for current imaging, *Microelectron. Reliab.* **41**, 1211 (2001).
- [34] Colin B. Clement, James P. Sethna, and Katja C. Nowack, Reconstruction of current densities from magnetic images by Bayesian Inference, preprint arXiv:1910.12929.
- [35] Eduardo A. Lima and Benjamin P. Weiss, Obtaining vector magnetic field maps from single-component measurements of geological samples, *J. Geophys. Res.* **114**, B06102 (2009).
- [36] Francesco Casola, Toeno van der Sar, and Amir Yacoby, Probing condensed matter physics with magnetometry based on nitrogen-vacancy centres in diamond, *Nat. Rev. Mater.* **3**, 17088 (2018).
- [37] Shaofen Tan, Yu Pei Ma, I. M. Thomas, and J. P. Wikswo, Reconstruction of two-dimensional magnetization and susceptibility distributions from the magnetic field of soft magnetic materials, *IEEE Trans. Magn.* **32**, 230 (1996).
- [38] S. Dreyer, J. Norpoth, C. Jooss, S. Sievers, U. Siegner, V. Neu, and T. H. Johansen, Quantitative imaging of stray fields and magnetization distributions in hard magnetic element arrays, *J. Appl. Phys.* **101**, 083905 (2007).
- [39] Yonathan Anahory, Jonathan Reiner, Lior Embon, Dorri Halbertal, Anton Yakovenko, Yuri Myasoedov, Michael L. Rappaport, Martin E. Huber, and Eli Zeldov, Three-junction SQUID-on-tip with tunable in-plane and out-of-plane magnetic field sensitivity, *Nano Lett.* **14**, 6481 (2014).
- [40] B. J. Maertz, A. P. Wijnheijmer, G. D. Fuchs, M. E. Nowakowski, and D. D. Awschalom, Vector magnetic field microscopy using nitrogen vacancy centers in diamond, *Appl. Phys. Lett.* **96**, 092504 (2010).
- [41] D. M. Feldmann, Resolution of two-dimensional currents in superconductors from a two-dimensional magnetic field measurement by the method of regularization, *Phys. Rev. B* **69**, 144515 (2004).
- [42] J.-P. Tetienne, N. Donschuk, D. A. Broadway, S. E. Lillie, T. Teraji, D. A. Simpson, A. Stacey, and L. C. L. Hollenberg, Apparent delocalization of the current density in metallic wires observed with diamond nitrogen-vacancy magnetometry, *Phys. Rev. B* **99**, 014436 (2019).

- [43] Matthew Pelliccione, Alec Jenkins, Preeti Ovarthaiyapong, Christopher Reetz, Eve Emmanouilidou, Ni Ni, and Ania C. Bleszynski Jayich, Scanned probe imaging of nanoscale magnetism at cryogenic temperatures with a single-spin quantum sensor, *Nat. Nanotechnol.* **11**, 700 (2016).
- [44] L. Thiel, D. Rohner, M. Ganzhorn, P. Appel, E. Neu, B. Müller, R. Kleiner, D. Koelle, and P. Maletinsky, Quantitative nanoscale vortex imaging using a cryogenic quantum magnetometer, *Nat. Nanotechnol.* **11**, 677 (2016).
- [45] K. Chang, A. Eichler, J. Rhensius, L. Lorenzelli, and Christian L. Degen, Nanoscale imaging of current density with a single-spin magnetometer, *Nano Lett.* **17**, 2367 (2017).
- [46] Mark J. H. Ku, Tony X. Zhou, Qing Li, Young J. Shin, Jing K. Shi, Claire Burch, Huiliang Zhang, Francesco Casola, Takashi Taniguchi, Kenji Watanabe, Philip Kim, Amir Yacoby, and Ronald L. Walsworth, Imaging Viscous Flow of the Dirac Fluid in Graphene Using a Quantum Spin Magnetometer. *Nature* (2020).
- [47] Scott E. Lillie, David A. Broadway, Nikolai Dontschuk, Sam C. Scholten, Brett C. Johnson, Sebastian Wolf, Stephan Rachel, Lloyd C. L. Hollenberg, and Jean-Philippe Tetienne, Laser modulation of superconductivity in a cryogenic wide-field nitrogen-vacancy microscope, *Nano Lett.* **20**, 1855 (2020).
- [48] J.-P. Tetienne, R. W. De Gille, D. A. Broadway, T. Teraji, S. E. Lillie, J. M. McCoe, N. Dontschuk, L. T. Hall, A. Stacey, D. A. Simpson, and L. C. L. L. Hollenberg, Spin properties of dense near-surface ensembles of nitrogen-vacancy centers in diamond, *Phys. Rev. B* **97**, 85402 (2018).
- [49] D. A. Broadway, N. Dontschuk, A. Tsai, S. E. Lillie, C. T.-K. Lew, J. C. McCallum, B. C. Johnson, M. W. Doherty, A. Stacey, L. C. L. Hollenberg, and J.-P. Tetienne, Spatial mapping of band bending in semiconductor devices using in situ quantum sensors, *Nat. Electron.* **1**, 502 (2018).
- [50] D. A. Broadway, B. C. Johnson, M. S. J. Barson, S. E. Lillie, N. Dontschuk, D. J. McCloskey, A. Tsai, T. Teraji, D. A. Simpson, A. Stacey, J. C. McCallum, J. E. Bradby, M. W. Doherty, L. C. L. Hollenberg, and J.-P. Tetienne, Microscopic imaging of the stress tensor in diamond using in situ quantum sensors, *Nano Lett.* **19**, 4543 (2019).
- [51] Timo Weggler, Christian Ganslmayer, Florian Frank, Tobias Eilert, Fedor Jelezko, and Jens Michaelis, Determination of the three-dimensional magnetic field vector orientation with nitrogen vacancy centers in diamond, *Nano Lett.* **20**, 2980 (2020).
- [52] David A. Simpson, Jean-Philippe Tetienne, Julia M. McCoe, Kumaravelu Ganesan, Liam T. Hall, Steven Petrou, Robert E. Scholten, and Lloyd C. L. Hollenberg, Magneto-optical imaging of thin magnetic films using spins in diamond, *Sci. Rep.* **6**, 22797 (2016).
- [53] D. Le Sage, K. Arai, D. R. Glenn, S. J. DeVience, L. M. Pham, L. Rahn-Lee, Mikhail D. Lukin, A. Yacoby, A. Komeili, and Ronald L. Walsworth, Optical magnetic imaging of living cells, *Nature* **496**, 486 (2013).
- [54] Edlyn V. Levine, Matthew J. Turner, Pauli Kehayias, Connor A. Hart, Nicholas Langellier, Raisa Trubko, David R. Glenn, Roger R. Fu, and Ronald L. Walsworth, Principles and Techniques of the Quantum Diamond Microscope, preprint arXiv:1910.00061.
- [55] D. Rohner, J. Happacher, P. Reiser, M. A. Tschudin, A. Tallaire, J. Achard, B. J. Shields, and P. Maletinsky, (111)-oriented, single crystal diamond tips for nanoscale scanning probe imaging of out-of-plane magnetic fields, *Appl. Phys. Lett.* **115**, 192401 (2019).
- [56] Shangjie Tian, Jian-Feng Zhang, Chenghe Li, Tianping Ying, Shiyang Li, Xiao Zhang, Kai Liu, and Hechang Lei, Ferromagnetic van der Waals Crystal VI 3, *J. Am. Chem. Soc.* **141**, 5326 (2019).
- [57] Suhan Son, Matthew J. Coak, Nahyun Lee, Jonghyeon Kim, Tae Yun Kim, Hayrullo Hamidov, Hwanbeom Cho, Cheng Liu, David M. Jarvis, Philip A. C. Brown, Jae Hoon Kim, Cheol Hwan Park, Daniel I. Khomskii, Siddharth S. Saxena, and Je Geun Park, Bulk properties of the van der Waals hard ferromagnet VI3, *Phys. Rev. B* **99**, 1 (2019).
- [58] Tai Kong, Karoline Stolze, Erik I. Timmons, Jing Tao, Danrui Ni, Shu Guo, Zoë Yang, Ruslan Prozorov, and Robert J. Cava, VI3—a new layered ferromagnetic semiconductor, *Adv. Mater.* **31**, 1 (2019).